Effect of RuO₂ in the Shape Selectivity of Submicron-Sized SnO₂ Structures

Niranjan S. Ramgir, Imtiaz S. Mulla,* and Kunjukrishna P. Vijayamohanan*

Physical and Materials Chemistry Division, National Chemical Laboratory, Pune - 411008, India

Received: November 22, 2004; In Final Form: April 16, 2005

Several dissimilar types of tin oxide microstructures including bipyramids, cubes, and wires synthesized effectively by means of a simple approach were investigated using X-ray diffraction (XRD), thermogravimetry/ differential thermometric analysis (TG-DTA), and X-ray photoelectron spectroscopy (XPS). A possible growth mechanism is proposed using the results of these studies. The texture coefficient values of all the structures, indexed to a tetragonal lattice, exhibit amazing variation in the preferred orientation with respect to their shapes. Although XPS data indicate that wires and cubes have a strong SnO₂ type signal, bipyramids interestingly exhibit both SnO and SnO₂ signals and a correlation of the binding energy helps in understanding the growth kinetics of such submicron structures. The results suggest that the bipyramids are formed because of the vapor−solid process (VS) while wires and cubes are formed by the vapor−liquid−solid (VLS) progression.

I. Introduction

The geometry of semiconducting oxides have a substantial effect on their optical,[1] electrical,[2] and gas-sensing[3] properties. Hence, an accurate control over the particle size and shape offers new application possibilities facilitating next generation materials with desired characteristics. Tin oxide, as a wide band gap semiconducting oxide, attracts an awesome interest because of its distinctive conductance properties. Two unique characteristics of tin oxide, that is, the variation of valence state and oxygen vacancy, make them useful for a variety of applications including gas sensors,[4] catalyst,[5] electrode material,[6] antireflecting coating,[7] and several other smart and functional devices. Consequently, in a short span of the past few years, various forms of tin oxide, namely, micro/nanowires,[8,9] nanotubes,[10] nanobelts,[11] nanodiskettes,[12] and meso/nanoporous[13,14] structures using diverse techniques such as thermal evaporation, laser ablation, carbothermal reduction, and solution precursor route, have been reported. All these studies clearly demonstrate that reduced dimensionality causes a radical change in the density of states highlighting the prominence of surface effects. Moreover, specific shape and the asymmetric interaction patterns on the surface of particles could induce orientation specific exchanges at lower dimensions. Besides size- and shape-dependent behavior, doping of these materials preserving the structural integrity can also provide a tool to tune their electronic properties. For example, doping can be used in the field of electronics for constructing contacts whose conductivity is governed by the level of doping.

Recently, we have demonstrated the shape selective synthesis of tin oxide in two different forms, namely, bipyramids (a double tetrahedron with a common plane, which is a natural habitat of rutile RuO₂ and SnO₂) and cubes along with microwires by employing RuO₂ as a promoter/nucleating agent.[15] The synthesis of these low dimensional building blocks is governed by a simple self-assembly process in which the prediction, precision, reliability, and instructions for assembly emerge from the nature of forces acting between the constituents.[16] Thus, to understand

the growth kinetics and to explore intellectual terra incognita further, we have carried out X-ray diffraction (XRD), thermogravimetric (TG-DTG), and X-ray photoelectron spectroscopic (XPS) studies of these low dimensional structures. The results of these investigations are presented below with the help of a plausible model describing the growth mechanism.

II. Experimental Section

(a) Materials. Tin(IV) oxide and ruthenium oxide were used as received from Aldrich.

(b) Characterization Techniques. XRD was carried out on a Rigaku, D/MAX IIIB diffractometer using Cu Kα radiation from a rotating anode X-ray generator operating at 30 kV and 15 mA at room temperature. The preferred orientation of the crystallographic planes was estimated by performing the Harris analysis.[17] The texture coefficient $P(h_i k_i l_i)$ and the preferred orientation of the $(h_i k_i l_i)$ planes were conferred by the following relationship:

$$P(h_i k_i l_i) = I(h_i k_i l_i)/I_o(h_i k_i l_i)\{(1/n) \sum I(h_i k_i l_i)/I_o(h_i k_i l_i)\}^{-1}$$
$$\text{for } i = 1, 2, 3... n \quad (1)$$

where $I(h_i k_i l_i)$ is the diffraction intensity of the $(h_i k_i l_i)$ plane of the sample under investigation, $I_o(h_i k_i l_i)$ is the intensity of the $(h_i k_i l_i)$ plane of the standard sample, and n is the number of reflections present.

Transmission electron microscopic (TEM) images were taken with a JEOL Model 1200 EX instrument operated at an accelerating voltage of 120 kV at room temperature. Scanning electron microscopic (SEM) measurements were carried out with a Leica Stereoscan-440 instrument equipped with a Phoenix energy dispersive analysis of X-ray (EDAX) attachment. The samples for TEM were prepared by directly sliding the Cu grid over the surface of as-deposited structures. Thermogravimetric analysis (TG-DTG) was carried out in the temperature range 323−1173 K under a Ar flow at a heating rate of 5 K/min on a Perkin-Elmer thermal analyzer. XPS measurements were performed using a VG Scientific ESCA-3 Mk II spectrometer, operating at a pressure of $>1 \times 10^{-9}$ Torr (pass energy of 50 eV, electron takeoff angle 60°, and overall resolution ~1 eV)

* To whom correspondence should be addressed. Tel: +91-020-5893300 ext 2270; fax: +91-020-5893044; e-mail: vk.pillai@ncl.res.in.
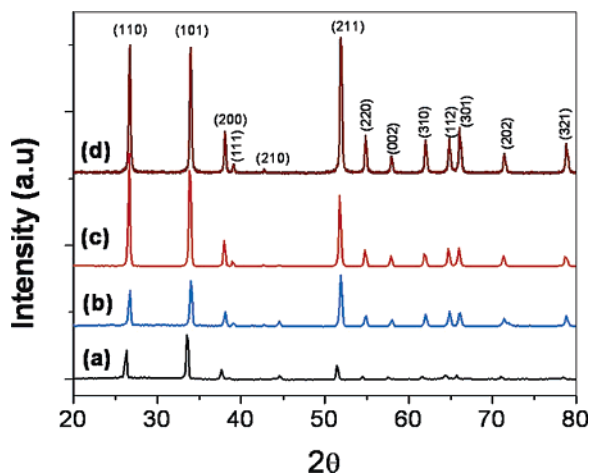
Figure 1. A comparison of XRD patterns of different forms of SnO₂: (a) bipyramids, (b) wires, (c) cubes, and (d) commercial SnO₂ (Aldrich 99.99%) exhibiting single-phase formation.

TABLE 1: The Texture Coefficient Values for the Different Structures Calculated Using the Harris Analysis (Eq 1)

		texture coefficient value		
sr. no	planes	wires	bipyramids	cubes
1	(110)	1.807	2.814	3.144
2	(101)	2.305	4.264	2.672
3	(200)	0.681	0.895	0.691
4	(211)	2.619	1.279	1.980

TABLE 2: Values of Lattice Constant, a (Å) and c (Å), a/c Ratio, Crystallite Size (nm) Calculated Using the Scherrer Equation; the Cell Volume (Å³) Is Also Indicated in the Last Column

sr. no	lattice parameters	bipyramids	wires	cubes	SnO₂-Aldrich
1	a (Å)	4.750(3)	4.782(3)	4.733(1)	4.730(1)
2	c (Å)	3.199(3)	3.183(3)	3.181(1)	3.183(1)
3	V (Å³)	72.2(1)	71.1(1)	71.29(4)	71.23(3)
4	a/c ratio	1.484	1.485	1.487	1.486
5	crystallite size (nm)	50.26	46.94	62.80	57.1
6	uniform strain (110)	6.08×10^{-3}	-7.75×10^{-3}	3.08×10^{-3}	

using a monochromatic MgKα source (energy $h\nu = 1253.6$ eV). The core level spectrum of the C 1s orbital was recorded with an overall instrumental resolution of ≈1 eV. The alignment of the binding energy was done using the Au 4f binding energy of 84 eV as a reference. The X-ray flux (power 70 W) was kept deliberately low to reduce the beam-induced damage. The spectra were fitted using a combined polynomial and Shirley type background function.[18,19]

III. Results and Discussion

Figure 1 shows XRD patterns of different forms of SnO₂ along with that obtained for commercial SnO₂ (Aldrich 99.99%).

The presence of characteristic tin oxide peaks, indexed to a tetragonal lattice, without any ruthenium oxide or mixed oxide, indicates single-phase formation. A comparison of the relative intensities of these samples with their standard values indicates the existence of a shape-dependent preferential growth in different planes. Interestingly, for bipyramids, cubes, and wires the preferential growths are in (101), (110), and (211) crystal directions, respectively (Table 1). We propose that such different shapes are triggered by the presence of RuO₂ along with the presence of metallic tin droplet acting together as nucleating
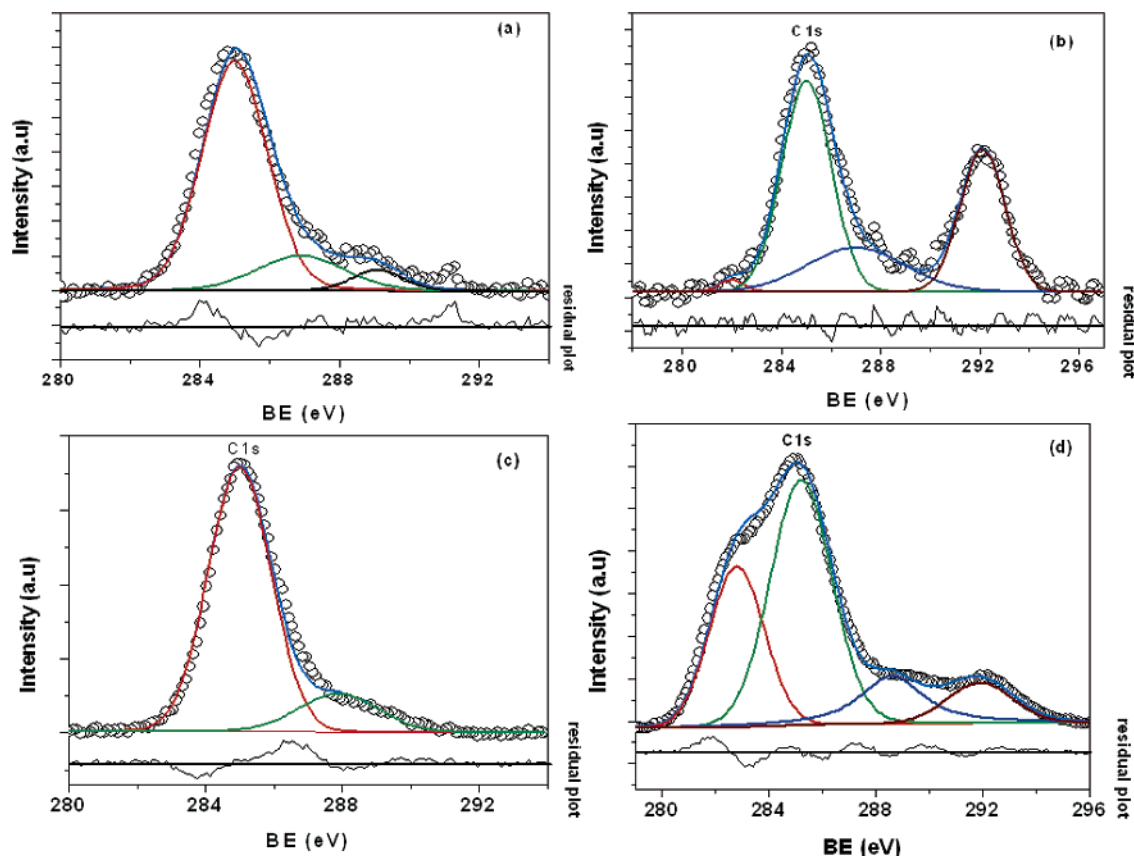

Figure 2. Deconvulated C 1s peaks for all the structures of tin oxide: (a) commercial SnO₂ (Aldrich 99.99%), (b) wires, (c) cubes, and (d) bipyramids. The minimal number of core level peaks and a combination of Shirley and linear backgrounds were chosen for each of the elements to produce random residuals (thin solid lines below fits).

TABLE 3: All the Binding Energy Positions of the Element Present in Different Submicron Structures of Tin Oxide

species	SnO$_2$-Aldrich	bipyramids	cubes	wires
			BE (eV)	
C 1s	285, 286.9, 289.1	285.2, 288.6, 291.9	285, 287.9	285, 287, 292.1
Ru 3d		282.8		282.0
Sn 3d	486.6, 495.1	484.5, 487.3, 493.5, 496.6	486.4, 494.9	486.1, 494.6
O 1s	530.7, 532.5 (minor)	529.6, 532.1, 534.1	530.5, 532.5 (minor)	530.3, 532.0 (minor)

aids. When all the SnO grains initially are embedded in RuO$_2$, the growth is supposed to trigger through a liquid droplet. This liquid droplet comprises a higher amount of RuO$_2$ and a lower amount of SnO and is likely to generate the reaction conditions directing the growth of SnO into wires, cubes, and bipyramids.

The lattice constants are further calculated to understand the strain-dependent properties. As depicted in Table 2, larger lattice parameters are observed for bipyramids (a = 4.750(3) Å and c = 3.199(3) Å) as compared with that of commercial SnO$_2$ (a = 4.730(1) Å, c = 3.183(1) Å), although no pronounced variation in lattice parameters, interestingly, is observed for cubes and wires. The unit cell volume for these structures suggests that for wires and cubes there is no dramatic variation while for bipyramids an increase in the cell volume by 1.3% is observed. The a/c ratio, which is a measure of lattice distortion, does not show any effective variation implying their stability.

An analysis of the effect of dopant on the electronic state of host material is of particular significance to understand the growth kinetics and, hence, XPS studies on all these structures were carried out. Accordingly, Figure 2 shows the deconvuluted C 1s peaks for all the structures of SnO$_2$. In all XP spectra, the hollow circles denote the original data while solid lines represent both the fitted curves and the deconvoluted individual peaks of different species. The residual of the fit of the spectra is also shown along with the results for comparison, and all binding energy positions of the elements are listed in Table 3. For commercial SnO$_2$, the spectrum can be deconvuluted into three peaks at 285, 286.9, and 289.1 eV corresponding to C 1s arising from the adsorbed carbon species. No signal corresponding to Ru (3d) is observed for commercial SnO$_2$ and cube samples, while for wires and bipyramids the peaks at 282.0 and 282.8 eV, respectively, confirm the presence of Ru in the "as-synthesized" submicron structures. These peaks can be attributed to RuO$_2$ signifying the binding energy of Ru 3d$_{5/2}$ corresponding to Ru^{4+} species.[20]

Commercial SnO$_2$, freshly prepared wires, as well as cubes exhibit two prominent peaks with a symmetric Voigt profile corresponding to the binding energies of Sn 3d$_{5/2}$ and Sn 3d$_{3/2}$, respectively (Figure 3). However, the presence of Sn^{2+} cannot be ruled out because the energy of Sn 3d$_{5/2}$ for SnO is very close to that for SnO$_2$ (0.7 eV). The peak-to-peak separation of Sn 3d peaks for commercial SnO$_2$ is 8.48 eV while for wires and cubes this amounts to 8.48 and 8.79 eV, respectively. For the bipyramids, four peaks at the binding energies (BEs) of 484.5, 487.3, 493.5, and 496.6 eV are observed corresponding to metallic Sn and SnO$_2$ 3d levels. The binding energy difference between the Sn^{4+} and Sn^o is 2.2 eV as in accordance with the literature values.[18] The broadening on the higher binding energy side of the peak can be attributed to the doping effect.

Figure 4 shows a comparison of O 1s signal for the commercial SnO$_2$ and freshly prepared wires and cubes, illustrating major peak maxima at BEs of 530.7, 530.3, and 530.5 eV, respectively, attributed to the lattice oxygen in the SnO$_2$ crystal structure.[21] There are minor contributions from

the adsorbed oxygen species, as revealed by the existence of minor peaks in Figure 4. In bipyramids, the single broad peak can be deconvulated into three peaks at BEs of 529.6, 532.1, and 534.0 eV corresponding to the oxygen of RuO$_2$, SnO$_2$ lattice, and the adsorbed species, respectively. Analysis of the difference between the binding energies of the Sn 3d$_{5/2}$ (E$_1$) and O 1s (E$_2$) electronic levels characterizing the Sn–O bond energy suggests that the incorporation of Ru in SnO$_2$ matrix does not have a noticeable change in the ΔE for wires and cubes. In contrast, for bipyramids, the change in the ΔE is 0.9 eV compared with that of commercial SnO$_2$, suggesting that Ru species in the bipyramidal structures alter the Sn–O bond energy. This is in accordance with the results of Rumyantseva et al. where a shift in ΔE has been observed when Ru is present in 1.1–1.2 at. %, thus further confirming the incorporation of Ru^{4+} into the Sn^{4+} positions.[18] Moreover, RuO$_2$ evaporates at low temperature as compared with SnO, and hence during the synthesis of bipyramids the vapors are assumed to be in excess of RuO$_2$ which are relocated through the carrier gas to the substrates kept downward, while the lower concentration of Ru left on the substrate acts as nucleating centers for the growth of wires and cubes. Thus, RuO$_2$ in its initial position acts as a nucleating center for structure growth that continues because of the self-catalyzed process pragmatic in the Sn–O system.
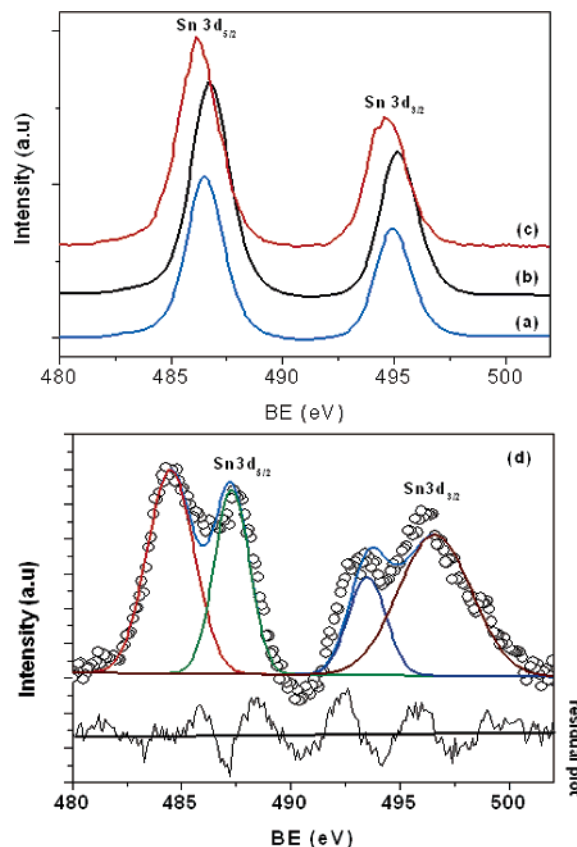

Figure 3. Comparison of the separate Sn 3d$_{5/2}$ and Sn 3d$_{3/2}$ signals for Sn in (a) cubes, (b) commercial SnO$_2$ (Aldrich 99.99%), (c) wires, and (d) bipyramids.
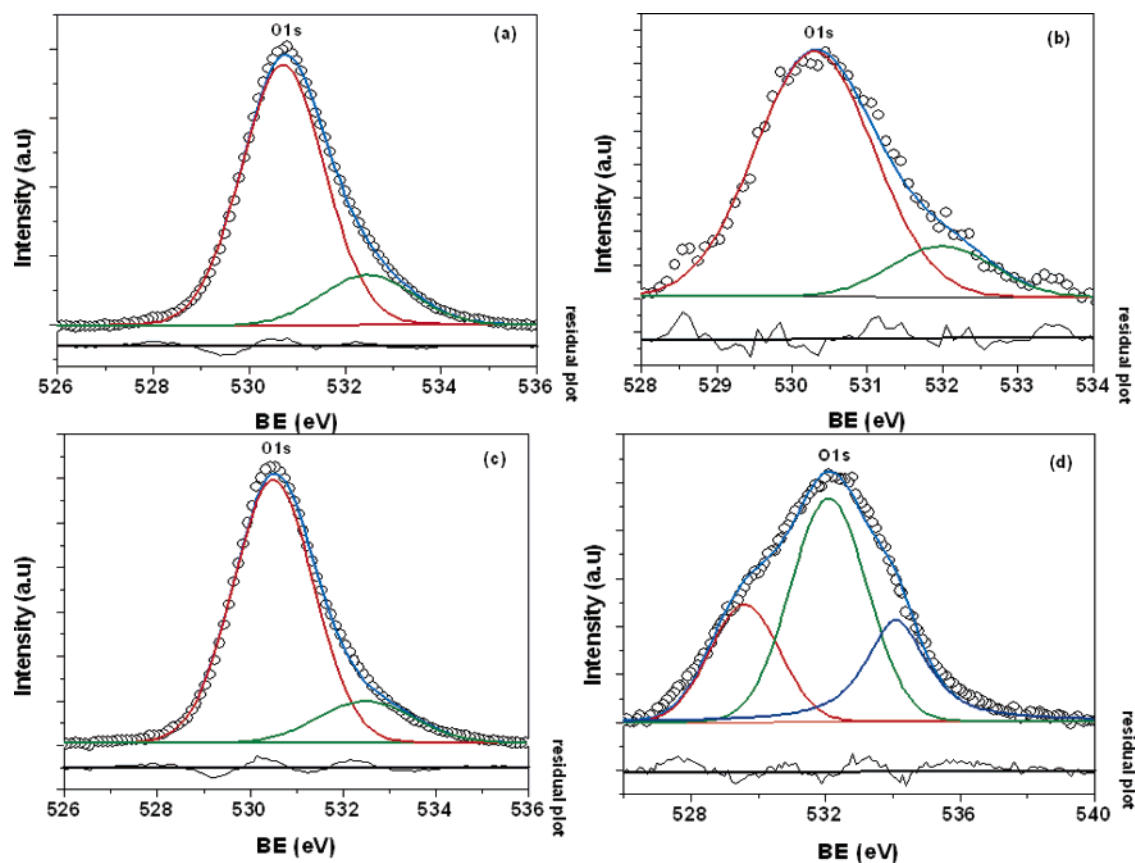
Figure 4. Comparison of the spectra for O 1s for different forms of SnO$_2$: (a) commercial SnO$_2$ (Aldrich 99.99%), (b) wires, (c) cubes, and (d) bipyramids.
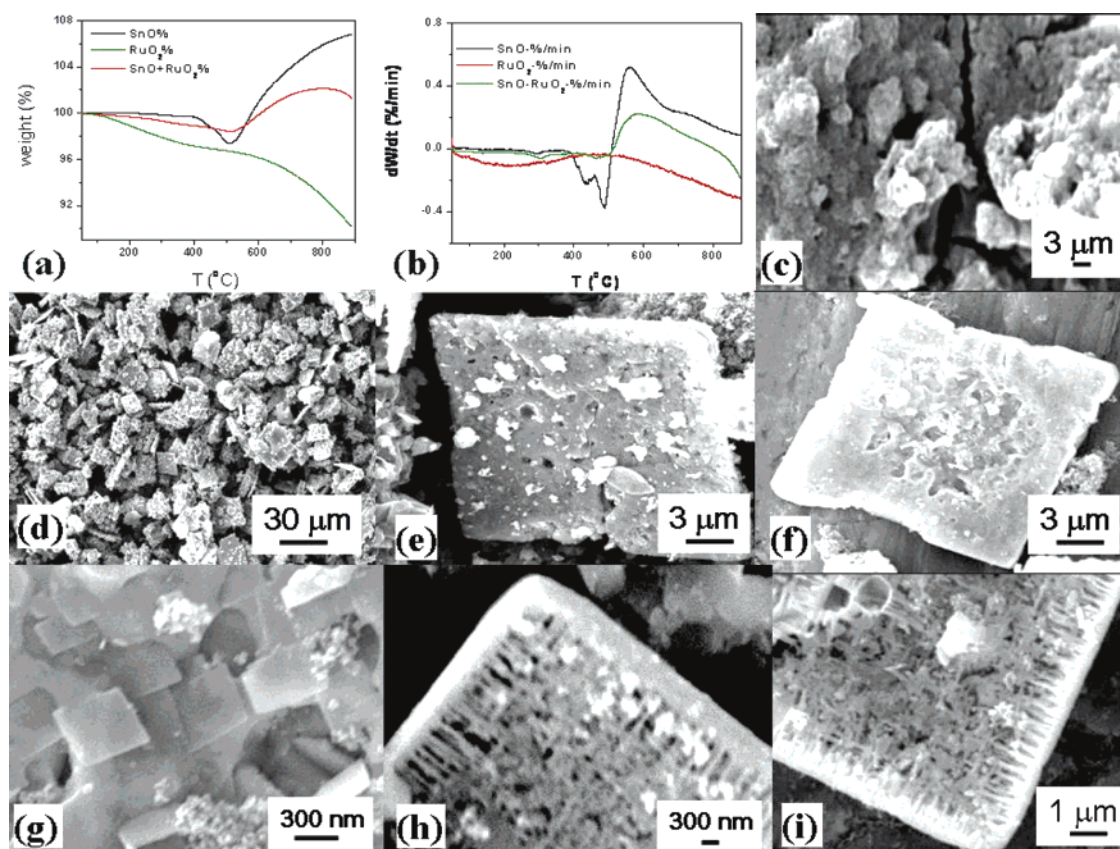

Figure 5. (a) TG and (b) DTA curves for the reaction mixture, pure SnO, and RuO$_2$ under Ar environment. SEM images of (c) pure RuO$_2$, (d−e) pure SnO, and the reaction mixture, showing (f−g) pyramid-like and (h−i) wirelike geometry within taken immediately after TGA-DTG studies.
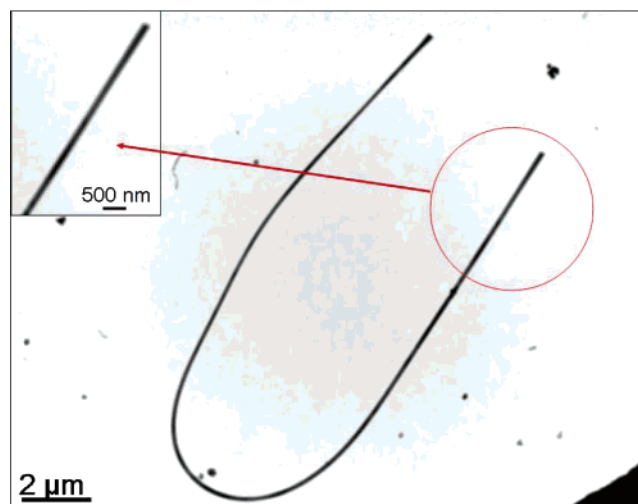
Figure 6. TEM image of a single wire, the spherical tip of which confirms the growth mode belonging to the vapor−liquid−solid process.

Moreover, the values of relative intensity of adsorbed oxygen are related with the grain size; the smaller the grain size, the higher the intensity of the adsorbed oxygen peak is. Thus, a comparison of the relative adsorbed oxygen peak intensities of all these structures suggests that the grain size decreases from cubes to bipyramids to wires, further supporting the conclusions derived from the XRD results.

To understand the role of RuO$_2$, we have carried out thermogravimetric (TG-DTG) studies of these structures. Figure 5 shows thermal profiles of the reaction mixture, pure SnO, and RuO$_2$ under Ar environment. Their SEM images taken immediately after TGA are also shown in order to correlate the morphology with weight loss. A gradual weight loss of 2.7% up to 510 °C is observed for pure SnO, which could be attributed to the formation of metallic tin droplets by the disproportion reaction

$$2SnO \rightarrow 2Sn + O_2 \qquad (2)$$

This is followed by a 7% increase in the mass up to 900 °C, owing to oxygen uptake and the formation of SnO$_2$ as per the equation

$$Sn + O_2 \rightarrow SnO_2 \qquad (3)$$

For pure RuO$_2$, a total weight loss of 10% is seen which could be attributed to the following reaction:

$$3RuO_2 \rightarrow Ru_3O_4 + O_2 \qquad (4)$$

For the reaction mixture containing SnO and RuO$_2$, however, a weight loss of 1.4% up to 520 °C (eqs 2 and 4) is observed followed by an increase in weight of about 2% up to 800 °C. Thus, the overall reaction could be expressed as

$$Sn + 3RuO_2 \rightarrow Ru_3O_4 + SnO_2 \qquad (5)$$
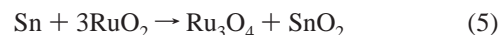
The appearance of a maximum at 800 °C suggests the predominance of eq 4 as compared with eq 2. Thus, it can be considered that metallic tin droplets are formed along with Ru$_3$O$_4$ inside the reaction chamber, and at high temperature and low oxygen partial pressure, they serve as both catalyst and active sites for SnO$_2$ vapor adsorption and subsequent SnO$_2$ deposition with Ru incorporation into the structure. The DTG analysis as depicted in Figure 5b shows two peaks for pure SnO at 435 and 487 °C, respectively, which correspond to the points of maximum slope on TG curves up to 561 °C, where the rate of weight change is minimum. The RuO$_2$ sample shows a peak around 210 °C, while the reaction mixture exhibits two peaks centered at 302 and 465 °C, respectively. The SEM images taken after the TG-DTG studies for pure RuO$_2$ do not show any distinct morphological changes, (Figure 5c), while in the case of pure SnO only cubical structures are observed (Figure 5d,

SCHEME 1:   Schematic Illustration of the Growth of Bipyramids along with Cubes (1a−c) and Wires (2a−c)[a]
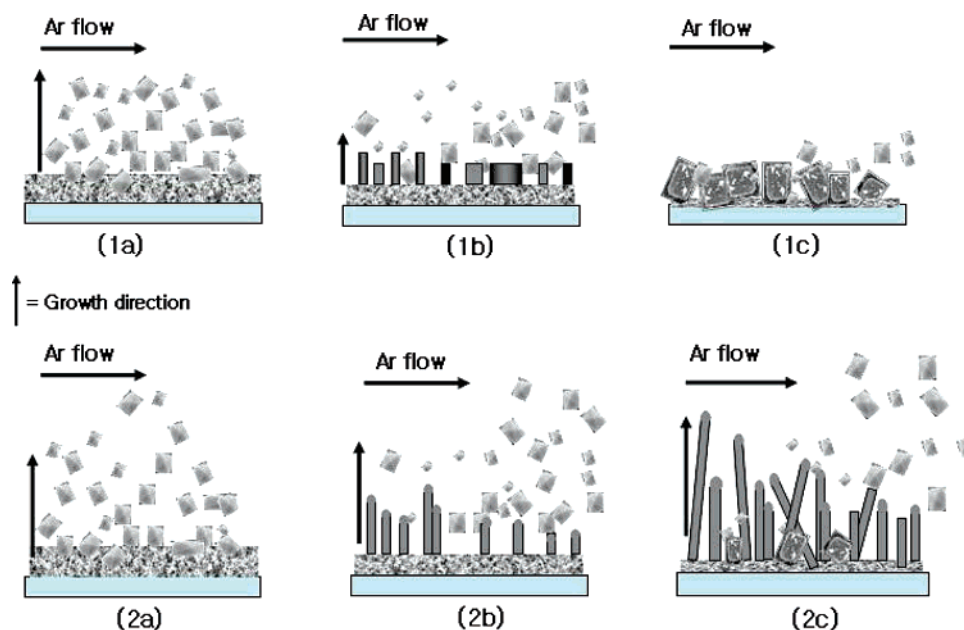
[a] (1a) Evaporation of the SnO and RuO$_2$ atoms at high temperature and the formation of bipyramids; (1b) scarcity of RuO$_2$ leading to insufficient growth of wires with low ambient pressure revealing the main mechanism of cube growth as absorption; (1c) formation of cubes whose envelop is given by the wires. (2a) Evaporation of the SnO and RuO$_2$ atoms at high temperature and the formation of bipyramids. (2b) Bipyramids are taken away by the carrier gas to the substrates kept downward and the initial growth of wires. (2c) When the ambient pressure is high, wires grow up mainly by the coalescence mechanism because of high probability of collisions among droplets, and the growth process is continued further by the self-catalyzed mechanism; the percentage of bipyramids on the surface decreases as they are carried away to the substrates kept downstream.
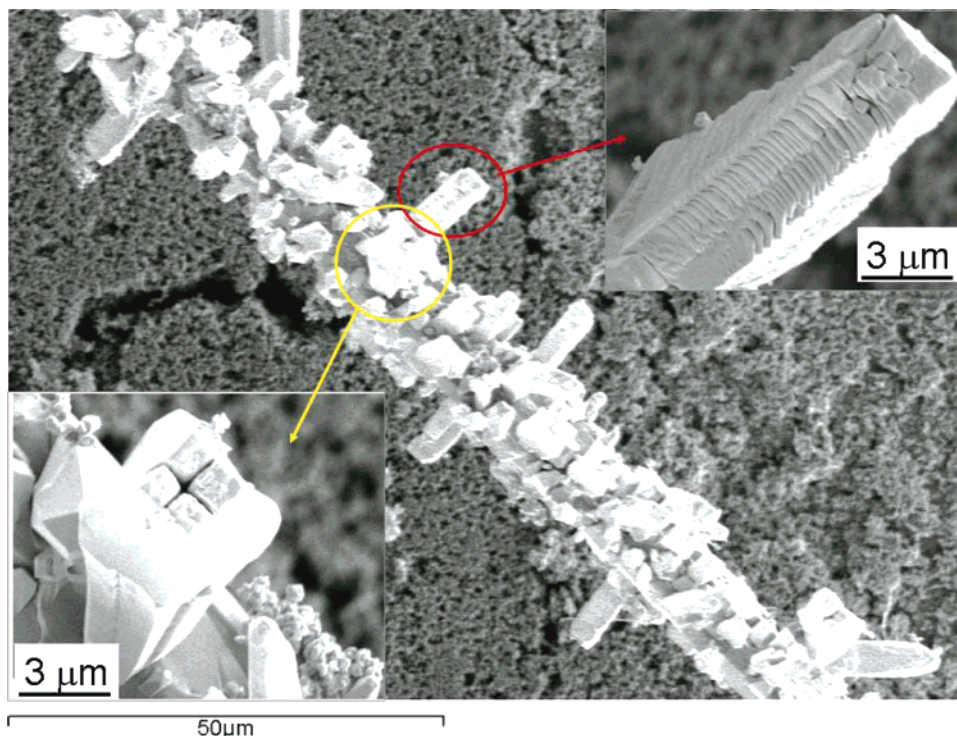
Figure 7. SEM images demonstrating the steps involved in the growth process. A single wire, on which different wires protrude out confirming the initiation of growth in all possible directions, is clearly indicated. Red circle: Stacking of cubical structures to give wires; yellow circle: simultaneous growth of four wires with traces of octahedral crystals.

e). In contrast, cubes with bipyramid (Figure 5f, g) and rodlike geometry within (Figure 5h, i) are observed for the reaction mixture indicating that the bipyramid and rod structures are likely to be formed in the beginning. However, being a static system, these structures grow further to attain cubical morphology with traces of bipyramids and wires persisting within. Our studies also demonstrate the significance of the amount and distribution of RuO_2 in the reaction mixture governing the shape selectivity during the growth process.

On the basis of the above experimental results, we propose a possible model for the growth, where atomic clusters, that is, aggregates of atoms or molecules, are in the size range from a few to thousands of the components. Their structural and electronic properties bear no resemblance either to the atoms they are composed of or to the solids or structures they can eventually grow.[22] The growth mechanism of 1D SnO_2 structures prepared by thermal evaporation is very well described by the vapor–liquid–solid (VLS) model.[23,24] It is assumed that metallic tin droplets act as catalysts as well as active sites for SnO_2 vapor adsorption and subsequent growth deposition as confirmed by the presence of spherical particles at the tip of these structures (Figure 6). Initially, all the SnO grains are assumed to be embedded in the RuO_2, and the growth process gets initiated via evaporation of a liquid droplet comprising higher concentration of RuO_2 and lower SnO. SnO_2 and RuO_2 both have natural habitats of octahedral and bitetragonal symmetries, and hence the vapors are most likely to be condensed in the bipyramidal form. In addition, the fraction of RuO_2 still residing on the substrate acts as a structure-directing agent, initiating the wire growth, which is sustained by the self-catalyzed growth process (Scheme 1, Figure 7). The carrier gas, Ar, carries the bipyramids to the substrates kept toward the downward stream where the temperature is between 200 and 500 °C. With a negligible amount of RuO_2 (6 wt %), the appearance of a biscuit-shaped cube suggests that the growth is initiated by the slow evaporation, perhaps directed upward.

As RuO_2 has higher vapor pressure, the lower concentration residing on the surface is insufficient for wire formation and hence gives favorable conditions for cube formation. The sharp edge to the cubical structure is given by the wires. (SI 1) Thus, the results confirm that the bipyramids are formed because of the vapor–solid process (VS) while wires and cubes are formed because of the vapor–liquid–solid (VLS) process. Interestingly, a change in the flow rate does not have a noticeable effect on the morphology of cubes or wires. On the other hand, experiments carried out with a different amount of RuO_2 in the reaction mixture clearly indicate that the yield of wire increases with RuO_2 content leading accordingly to the decrease in the cubical structures.

IV. Conclusion

We have clearly demonstrated the shape selective synthesis of different forms of submicron-sized tin oxide bipyramids, cubes, and wires using RuO_2 as a unique catalyst. These forms represent promising candidates for both further studies of low dimensional physics and enormous applications in various fields such as nanoelectronics, nanostructured sensors, and so forth. The present study indicates the key role of RuO_2 as an important nucleating agent in promoting the growth of low dimensional structures of tin oxide. Further, XRD, TG-DTA, and XPS studies elucidate the interactions between the nuclei of the building blocks (RuO_2 and SnO liquid droplets), which are critically controlled by the presence of carrier gas and the amount of RuO_2 in the initial reaction mixture. Moreover, such interactions are extremely helpful in understanding how specific types of reactions are responsible for specific target structures as demonstrated where their formation is particularly governed by the kinetics. Thus, the shape-dependent preferential growth directions observed in tin oxide microstructures indicates that a control over growth position and shape could be achieved by tuning the location and amount of Ru.

Supporting Information Available: SI 1 SEM images of cubes showing the sharp edges governed by the wires that are formed. This material is available free of charge via the Internet at http://pubs.acs.org.

References and Notes

(1) Wang, X. D.; Summers, C. J.; Wang, Z. L. *Nano Lett.* **2004**, *4*, 423.

(2) Wang, J.-G.; Tian, M.-L.; Mallouk, T. E.; Chan, M. H. W. *Nano Lett.* **2004**, *4* (7), 1313.

(3) Niranjan, R. S.; Sainkar, S. R.; Vijayamohanan, K.; Mulla, I. S. *Sens. Actuators, B* **2002**, *82*, 82.

(4) Chaudhary, V. A.; Mulla, I. S.; Vijayamohanan, K.; Hegde, S. G.; Srinivas, D. *J. Phys. Chem. B* **2001**, *105* (13), 2565.

(5) Harrison, P. G.; Bailey, C.; Bowering, N. *Chem. Mater.* **2003**, *15* (4), 979.

(6) Gaudet, J.; Tavares, A. C.; Trasatti, S.; Guay, D. *Chem. Mater.* **2005**, *17* (6), 1570.

(7) Aegerter, M. A.; Reich, A.; Ganz, D.; Gasparro, G.; Putz, J.; Krajewski, T. *J. Non-Cryst. Solids* **1997**, *218*, 123.

(8) Kijima, T.; Ikeda, T.; Yada, M.; Machida, M. *Langmuir* **2002**, *18* (16), 6453.

(9) Nguyen, P.; Ng, H. T.; Kong, J.; Cassell, A. M.; Quinn, R.; Li, J.; Han, J.; McNeil, M.; Meyyappan, M. *Nano Lett.* **2003**, *3* (7), 925.

(10) Liu, B.; Zeng, H. C. *J. Phys. Chem. B* **2004**, *108* (19), 5867.

(11) Comini, E.; Guidi, V.; Malagu, C.; Martinelli, G.; Pan, Z.; Sberveglieri, G.; Wang, Z. L. *J. Phys. Chem. B* **2004**, *108* (6), 1882.

(12) Dai, Z. R.; Gole, J. L.; Stout, J. D.; Wang, Z. L. *J. Phys. Chem. B* **2002**, *106* (6), 1274.

(13) Srivastava, D. N.; Chappel, S.; Palchik, O.; Zaban, A.; Gedanken, A. *Langmuir* **2002**, *18* (10), 4160.

(14) Kolmakov, A.; Zhang, Y.; Moskovits, M. *Nano Lett.* **2003**, *3* (8), 1125.

(15) Ramgir, N. S.; Mulla, I. S.; Vijayamohanan, K. P. *J. Phys. Chem. B* **2004**, *108*, 14815.

(16) Zhang, Z.; Glotzer, S. C. *Nano Lett.* **2004**, *4*, 1407.

(17) Mazher, J.; Shrivastav, A. K.; Nandedkar, R. V.; Pandey, R. K. *Nanotechnology* **2004**, *15*, 572.

(18) Borchert, H.; Talapin, D. V.; Goponik, N.; McGinley, C.; Adam, S.; Lobo, A.; Moller, T.; Weller, H. *J. Phys. Chem. B* **2003**, *107*, 9662.

(19) The spectras were fitted using the software XPSPEAK4.1 which is available free on website www.uksaf.org/software.html#7. The peak fitting was accepted with $\Sigma\chi^2 \leq 80$.

(20) Rumyantseva, M. N.; Safanova, O. V.; Boulova, M. N.; Ryabova L. I.; Gaskov, A. M. *Russ. Chem. Bull. Int. Ed.* **2003**, *52*, 1217.

(21) Egdell, R. G.; Rebane, J.; Walker, T. J.; Law, D. S. L. *Phys. Rev. B* **1999**, *59*, 1792.

(22) Wang, Z. L.; Liu, Y.; Zhang, Z. *Handbook of Nanophase and Nanostructured Materials*; Kluwer Academic/Plenum US Publishers: New York, 2002; Vol. 3, p 1.

(23) Ding, Y.; Gao, P. X.; Wang, Z. L. *J. Am. Chem. Soc.* **2004**, *126* (7), 2066.

(24) Gao, P. X.; Wang, Z. L. *J. Phys. Chem. B* **2004**, *108* (23), 7534.